energies

MDPI

Article

One-Pot Fast Electrochemical Synthesis of Ternary Ni-Cu-Fe Particles for Improved Urea Oxidation

Marta Wala-Kapica [1,*], Aleksander Gąsior [2], Artur Maciej [2], Szymon Smykała [3], Alicja Kazek-Kęsik [2], Mehdi Baghayeri [2,4] and Wojciech Simka [2,*]

[1] Faculty of Mechanics, Wroclaw University of Science and Technology, 50-370 Wroclaw, Poland
[2] Faculty of Chemistry, Silesian University of Technology, 44-100 Gliwice, Poland
[3] Faculty of Mechanics and Technology, Silesian University of Technology, 44-100 Gliwice, Poland
[4] Department of Chemistry, Faculty of Science, Hakim Sabzevari University, Sabzevar 96131, Iran
* Correspondence: marta.wala-kapica@pwr.edu.pl (M.W.-K.); wojciech.simka@polsl.pl (W.S.)

Abstract: The climate crisis has become the most serious concern of human beings and environments worldwide in the 21st century. Global concerns about cancer epidemiology mainly originate from anthropogenic activities, particularly fossil-based operations. A key solution to this problem is the use of fuel cells—devices—capable of the direct conversion of fuel chemical energies like urea into electricity. To make their commercialization reasonable, one of the problems that needs to be solved is the development of anodic materials. The majority of investigations on urea oxidation are based on nickel, but its inadequate activity limits the efficiency of these devices. In this work, we propose and synthesize a Ni-Cu-Fe ternary electrocatalyst for urea oxidation through a fast and facile electrodeposition method. The properties of the synthesized material are examined by Scanning Electron Microscopy (SEM) conjugated with Energy Dispersive X-ray Spectroscopy (EDS), Transmission Electron Microscopy (TEM), and X-ray Diffraction (XRD). Its electrochemical properties were also examined in a 1 M KOH solution with and without 0.15 M urea. We found that the prepared powder is active in the electro-oxidation of urea, with 1.65 $V_{vs\ RHE}$ required for a current density of 10 mA cm^{-2} and a stable potential of 2.38 $V_{vs\ RHE}$ required for 3 h of polarization at 10 mA cm^{-2}.

Keywords: environmental protection; fuel cell; urea oxidation; electrodeposition; electrocatalyst

check for updates

Citation: Wala-Kapica, M.; Gąsior, A.; Maciej, A.; Smykała, S.; Kazek-Kęsik, A.; Baghayeri, M.; Simka, W. One-Pot Fast Electrochemical Synthesis of Ternary Ni-Cu-Fe Particles for Improved Urea Oxidation. *Energies* **2024**, *17*, 5455. https://doi.org/10.3390/en17215455

Academic Editor: Claudio Mele

Received: 9 October 2024
Revised: 25 October 2024
Accepted: 29 October 2024
Published: 31 October 2024

Copyright: © 2024 by the authors. Licensee MDPI, Basel, Switzerland. This article is an open access article distributed under the terms and conditions of the Creative Commons Attribution (CC BY) license (https://creativecommons.org/licenses/by/4.0/).

1. Introduction

The worldwide increase in demand for green and sustainable electricity takes its origin in the need for a global paradigm shift from crude-oil- and natural-gas-based operations and economies towards a circular economy based on sustainable materials and energy resources. Fuel cells are devices enabling the direct conversion of the chemical energy resulting from chemical bonds in fuel molecules to electricity via a redox reaction. As a result of such a reaction, similar to conventional gasoline or diesel engines, fuel is oxidized, but the energy loss related to the change of the heat energy to kinetic energy can be avoided. Another solution to the hazardous emissions of fossil-based energy devices is replacing them with green and sustainable energy-saving devices based on environmentally friendly substances, such as urea, simple alcohols, or ammonia, to be used as green fuel [1,2].

The commercialization of direct fuel cells would be very beneficial from an environmental point of view. In 2023, the European Union planned to ban the sale of new cars emitting CO_2 by 2035, pursuing the Net Zero emission horizon [3]. With the growing popularity and worldwide acceptance of electric vehicles, the disadvantages of using lithium-ion batteries, like how easily they catch fire, have become more and more identified to the public as well as to decision-making organizations. However, the use of fuel cells for electricity generation in combination with an electric engine could still lure the attention of enterprises, because this approach is much more beneficial than the use of batteries. Furthermore, fuel cells are lighter than batteries, which seems very beneficial from

a modern engineering point of view; additionally, they can be stored in a fuel tank, similar to those used in combustion engines. Due to the fact that long stops related to battery charging can be eliminated on long journeys and due to the already existing infrastructure costs of switching from gasoline and diesel petrol to more environmentally friendly liquid alternatives, such as simple alcohols or urea, there can be a smooth transition [2,4,5].

One of the holdbacks of the commercialization of direct fuel cells, such as the Direct Urea Fuel Cell (DUFC), is the lack of proper anodic materials. The requirements the final material must meet are wide, like it must not only be active enough and cheap in production, but also maintain its activity during use [6–8].

The standard material in urea oxidation research is nickel, a metal that can create the latter of its hydroxide in alkaline environments, which later, after an application of proper potential, can be turned to its oxyhydroxide, which is an active agent for urea oxidation. Unfortunately, nickel itself does not have activity high enough to make the use of fuel cells commercially reasonable. Different approaches have been examined to increase its activity, from the use of nickel in the form of nanomaterials to doping it with different elements and the preparation of metal organic frameworks (MOFs) [9–12].

Among popular nickel dopants, iron is a very interesting element, which can be used as a dopant for nickel electrocatalysts because of its low price, related to its high abundance on Earth. Additionally, this metal is vital for living organisms, so it is non-toxic to living organisms [13–15].

The main challenge in the preparation of the industrial-scale demand for anodic materials using popular hydrothermal methods is their price and time consumption. The solution to these problems may be the preparation of catalytic materials using the electrodeposition process. This well-known technology provides a high degree of process control from the composition of the final material to the size of the prepared particles by controlling the electrical parameters of the process [16–18].

Our approach is a mix of two mentioned above: we prepared an electrocatalyst consisting of nickel doped with copper and iron using the electrodeposition process from an electrolytic bath, which has not been described previously. The physiochemical properties of the obtained powder were examined using Scanning Electron Microscopy (SEM), Transmission Electron Microscopy (TEM), and X-ray Diffraction (XRD). The electrochemical properties of the prepared materials were examined using cyclic voltammetry (CV) and chronoamperometry (CA). The obtained material shows activity towards urea oxidation, with 1.65 $V_{vs\ RHE}$ required for 10 mA cm^{-2} and a stable potential of 2.38 $V_{vs\ RHE}$ required for 3 h of polarization to 10 mA cm^{-2}.

2. Materials and Methods

2.1. Material Synthesis

All chemicals used, nickel sulphate, copper sulphate, iron sulphate, sodium citrate, ammonia, potassium hydroxide and urea, were of analytical purity and were purchased from the Avantor (Gliwice, Poland).

The samples were prepared by applying an electrodeposition process in an electrolytic bath containing nickel copper and iron salts with the concentration described in Table 1. After dissolving all the electrolytic bath ingredients, the pH was regulated using a 25% ammonia solution, which was added while stirring until a pH of 4 was reached.

Table 1. Ingredients used in preparation of the solution for the electrolytic bath.

Ingredient	Concentration
$NiSO_4$	0.375
$CuSO_4$	0.125
$FeSO_4$	0.100
Sodium citrate	0.200

The chosen electrolytic bath was prepared according to [19], but it was modified by the addition of iron sulphate and the change of the pH to acidic, which are steps that have not been described before in the literature.

Procedures for electrodeposition of catalytic powder have previously been described for similar material [20]. Briefly, the powders were electrodeposited on copper plates, which were already ground before the process using SiC grinding paper of grade 800 and 1000, followed by cleaning with deionized water and degreasing in isopropanol using ultrasound for 5 min. Prior to the electrodeposition process, the plates' surfaces were also activated by dipping them in a 40% HNO_3 solution for 60 s. Immediately after the acid treatment, the samples were rinsed with deionized water and immersed in the electrolytic bath. The electrodeposition process was conducted in an electrolyser equipped with a mechanical stirrer and nickel anodes. The copper plate on which the powder was deposited played the role of the cathode. The current density used was 20 A dm^{-2}. After the electrodeposition, the prepared powders were taken off the copper plate using ultrasound in isopropanol. After the ultrasound treatment, the isopropanol was evaporated, and the resulting powders were collected, stored, and later used for further studies.

2.2. Material Characterization

The morphology and elemental composition of the samples was examined using a Phenom ProX (Thermo Fischer Scientific, Phenom World, Eindhoven, The Netherlands) Scanning Electron Microscope (SEM) equipped with an Energy Dispersive X-ray Spectroscopy (EDS) gun. An accelerating voltage of 15 kV was used.

Observations of the morphology and nanostructure of the synthesized materials were performed by using a Titan 80–300 (Thermo Fischer Scientific, FEI, Hillsboro, OR, USA) Transmission Electron Microscope (TEM) operating at an accelerating voltage of 300 kV. The images and selected area electron diffraction (SAED) patterns were acquired in TEM mode under parallel beam illumination. The analysed powders were fist-sonicated in ethanol. After a sufficient dispersion was obtained, one droplet of suspension was deposited on a copper TEM grid covered with a lacey carbon film. Prior to examination, for the removal of any organic contamination, the samples were treated for 3 s in argon plasma using 1020 Plasma Cleaner (E.A. Fischione Instruments, Inc., Export, PA, USA).

The phase composition of the samples was determined using a Seifert 3003 TT (RICH. SEIFERT & Co. GmbH & Co. KG, Ahrensburg, Germany) powder X-ray Diffractometer with a Cu X-ray tube ($k\lambda_1$ = 1.540598 Å, $k\lambda_2$ = 1.544426 Å, $k\beta$ = 1.39225 Å), and the powder samples were analysed three times. The samples were insensitive towards X-rays, and the results are presented as an average of the scans between 5° and 80° 2θ (step size = 0.05°).

2.3. Electrochemical Characterization

To examine the electrochemical properties of the prepared powders, catalytic ink was formulated, containing 33.3 mg of powder per 1 mL of isopropanol and a water mixture with the addition of Nafion® solution. After mixing the powder with liquids, the ink was homogenized for 1 h using ultrasound until a deep, black suspension was formed. After homogenization, 5 µL of the ink was deposited on the polished surface of the glassy carbon and dried overnight. The procedure is shown in Figure 1.

Electrochemical measurements were conducted using PARSTAT 4000A (Ametek, Princeton Applied Research, Berwyn, PA, USA) and the dedicated Versa Studio software (v. 2.52.3). The prepared sample played the role of a working electrode; a glassy carbon rod was used as a counter electrode, and the Ag | AgCl electrode filled with saturated potassium chloride was used as a reference electrode.

To make the comparison between different materials easier, all potentials in this paper are given in regard to a Reversible Hydrogen Electrode (RHE). The calculations were based on Equation (1) [21]:

$$E_{RHE} = E_{Ag|AgCl(sat\ KCl)} + E^0_{Ag|AgCl(sat\ KCl)} + 0.059 \cdot pH \quad (1)$$

where $E^0_{Ag|AgCl(sat\ KCl)}$ is the standard potential of the $Ag\,|\,AgCl_{(sat\ KCl)}$ electrode (0.197 V) [21].

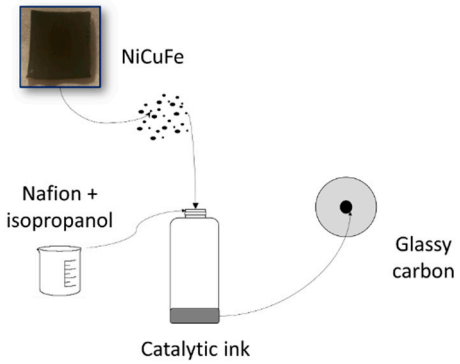


Figure 1. Schematic of the working electrode preparation used in this study.

The first step of examining the material activity was related to the selection of the potassium hydroxide concentration. Three solutions of concentrations of 0.5, 1, and 2 moles of KOH per litre were used. The activity of the prepared samples was examined using cyclic voltammetry (CV) with a scan rate of 10 mV s^{-1} in the voltage range of 0 to 0.75 V vs. $Ag\,|\,AgCl_{(sat\ KCl)}$.

The activity of the prepared powder toward urea oxidation was examined in a 1 M KOH + 0.15 M urea solution. The chosen concentration of the urea is proportional to the urea content in human urine, which is close to 0.33 M, but after adjusting to a proper pH for a Ni-based catalyst, it resulted in being diluted down.

As in the KOH solutions without the addition of urea, the activity of the prepared material was examined using cyclic voltammetry in the voltage range of 0 to 0.75 V vs. $Ag\,|\,AgCl_{(sat\ KCl)}$ with a scan rate of 10 mV s^{-1}.

An Electrochemical Impedance Spectroscopy (EIS) examination was conducted in both 1 M KOH and 0.15 M urea in 1 M KOH solutions using the same experimental setup as the rest of electrochemical measurements. Prior to the measurement, each sample was polarized to the potential of 1.32 $V_{vs\ RHE}$ for 10 min to stabilize. After that, the EIS measurement was conducted in the frequency range from 10^5 to 5×10^{-3} Hz using an amplitude of 10 mV. Registered data were fitted to the equivalent circuits using ZSimpWin software (version 3.60).

The stability of the prepared material was examined using chronoamperometry measurements (CA), where the samples were polarized for 30 min to the potential registered as the anodic peak potential during CV scans in the solution containing urea.

The stability of the proposed material was also examined by its polarization to a current density of 10 mA cm^{-2} and the recording of the resulting potential.

To examine the durability of the proposed catalyst, multiscan CV measurements were performed. Twenty subsequent scans in the voltage range from 0 to 0.75 V vs. $Ag\,|\,AgCl_{(sat\ KCl)}$ with a scan rate of 10 mV s^{-1} were conducted.

3. Results

3.1. SEM + EDX

The morphology of the prepared samples provides support for the used synthesis protocol [20,22]. It is apparent in Figure 2 that, as a result of the high current density during the electrodeposition process simultaneously with metal deposition, hydrogen gas bubbles are formed on the surface of the cathode. Actually, the bubbles that are formed on the surface of the material are playing the role of a dynamic template before they grow big enough to detach from the cathode. The entire bubble life cycle takes very little time, which makes it a perfect way to prepare electrocatalytic powders with a high active surface [22].

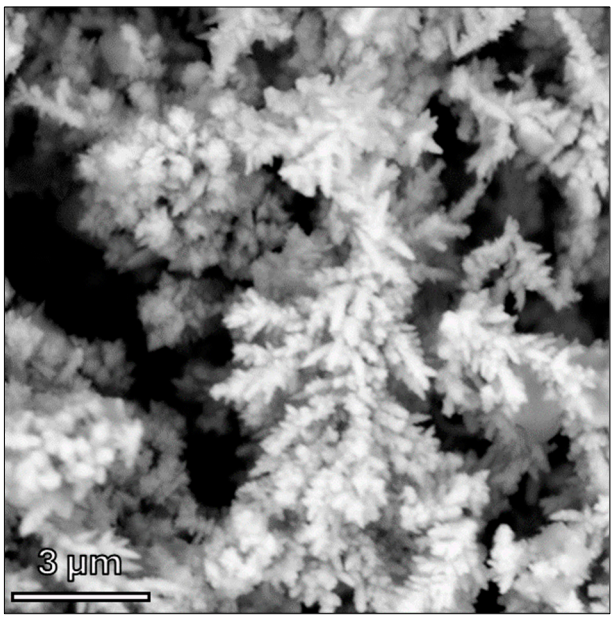


Figure 2. SEM image of the prepared Ni-Cu-Fe powder.

In Figure 2, an SEM image of the prepared powder is presented, which resembles a pine tree covered by snow. The obtained coral-like dendrite (Greek. *Dendron*—tree [23]) shape shows primary branches present in the centre of a particle, secondary branches radiating outwards, and ramifications to even smaller structures as the distance from the primary branch is growing. Such morphology suggests that the prepared ternary Ni-Cu-Fe material should have a high active surface, which would be a very beneficial feature considering that the catalysis is a surface process [24,25].

Figure 3 shows the EDS mapping of the prepared ternary metallic material. The results of the conducted analysis showed that all of the metals present in the electrocatalytic bath were present in the final material. The evenly distributed domains, observed in the images and approved by EDS mapping, suggest that the proposed electrolytic bath was well balanced. The most abundant element was nickel (61 $\pm$ 4%), followed by copper (22 $\pm$ 2%) and iron (10 $\pm$ 1%). The rest of the elemental composition of the material was other elements present in the electrolytic bath, such as sulphur and sodium.

3.2. XRD

In Figure 4, the XRD spectrum observed for the Ni-Cu-Fe sample is shown. Characteristic peaks related to the presence of a $Cu_{0.51}Ni_{0.49}$ alloy phase and the presence of an $FeNi_3$ alloy phase are visible. This means that during the electrodeposition process, Ni, Cu, and Fe were deposited in the form of two separate alloy phases instead of solely one or any discrete deposition of each metal.

Due to the similarity of the electrolytic bath and the process of synthesis, our materials should exhibit a similar composition as NiCu described previously [26], which is Cu2p and Ni2p, present in the form of their oxide nanoparticles with defects. The proposed material is most likely composed of nanoparticles of oxides, which formed it.

It is known that the addition of another metal to the electrocatalyst can improve its activity due to the changes in the electronic structure. The electron transfer can be promoted during the reaction [27], i.e., MoO_2 added to $NiCo_2$ improves its activity towards 5-Hydroxymethylfurfural (HMF) oxidation or leads to charge redistribution, which affects the adsorption of reaction substrates like urea or hydroxide ions [28,29]. The positive influence of copper oxide on nickel hydroxide leading to charge redistribution and thus improving the material's electrocatalytic properties was also confirmed by Density Functional Theory (DFT) [30].

Weaker Lewis acids such as Cu and Fe can shift the antibonding state of Ni toward the Fermi level, which leads to a downshift in the nickel D-band centre and thus decreases the Ni redox potential, facilitating its oxidation to NiOOH [29,31].

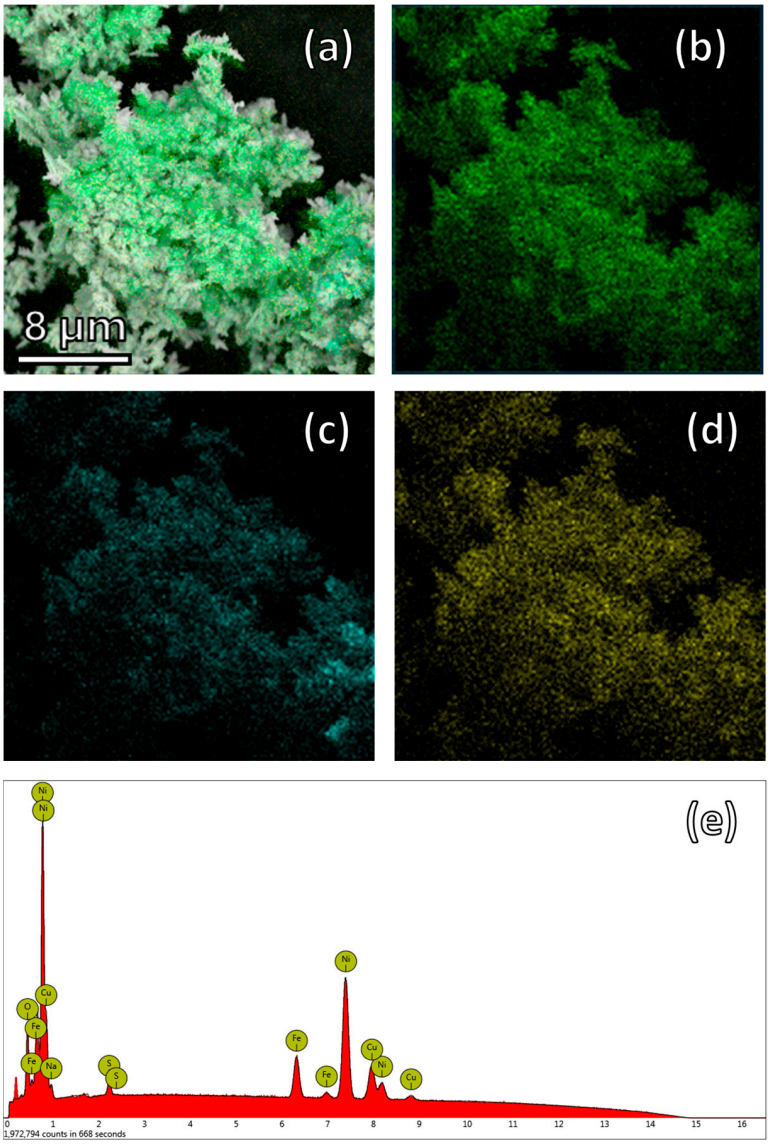


Figure 3. EDS map of the prepared material (**a**) with maps related to the presence of nickel (**b**), copper (**c**), and iron (**d**) with the EDS spectra (**e**).

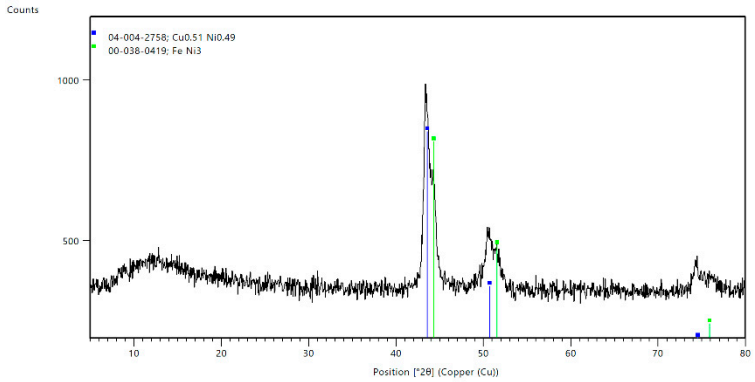


Figure 4. XRD spectra of the prepared Ni-Cu-Fe ternary powder.

3.3. TEM

Based on TEM observations, we were able to capture relevant information about the powder's morphology and structure. Even after being subjected to sonication, the obtained material consisted mainly of particles with sizes of several micrometres (Figure 5a). Observations at higher magnifications revealed a highly developed surface with dendrite-like structures (Figure 5b). The obtained SAED patterns (PDF card no. 04-004-2758 for $Cu_{0.51}Ni_{0.49}$ and card no. 00-038-0419 for $FeNi_3$) show that the powder agglomerates consist of highly polycrystalline regions (Figure 5c) as well as bulk monocrystals (Figure 5d). High-resolution imaging further confirmed the presence of both polycrystalline (Figure 5e) and bulk monocrystal (Figure 5f) areas.

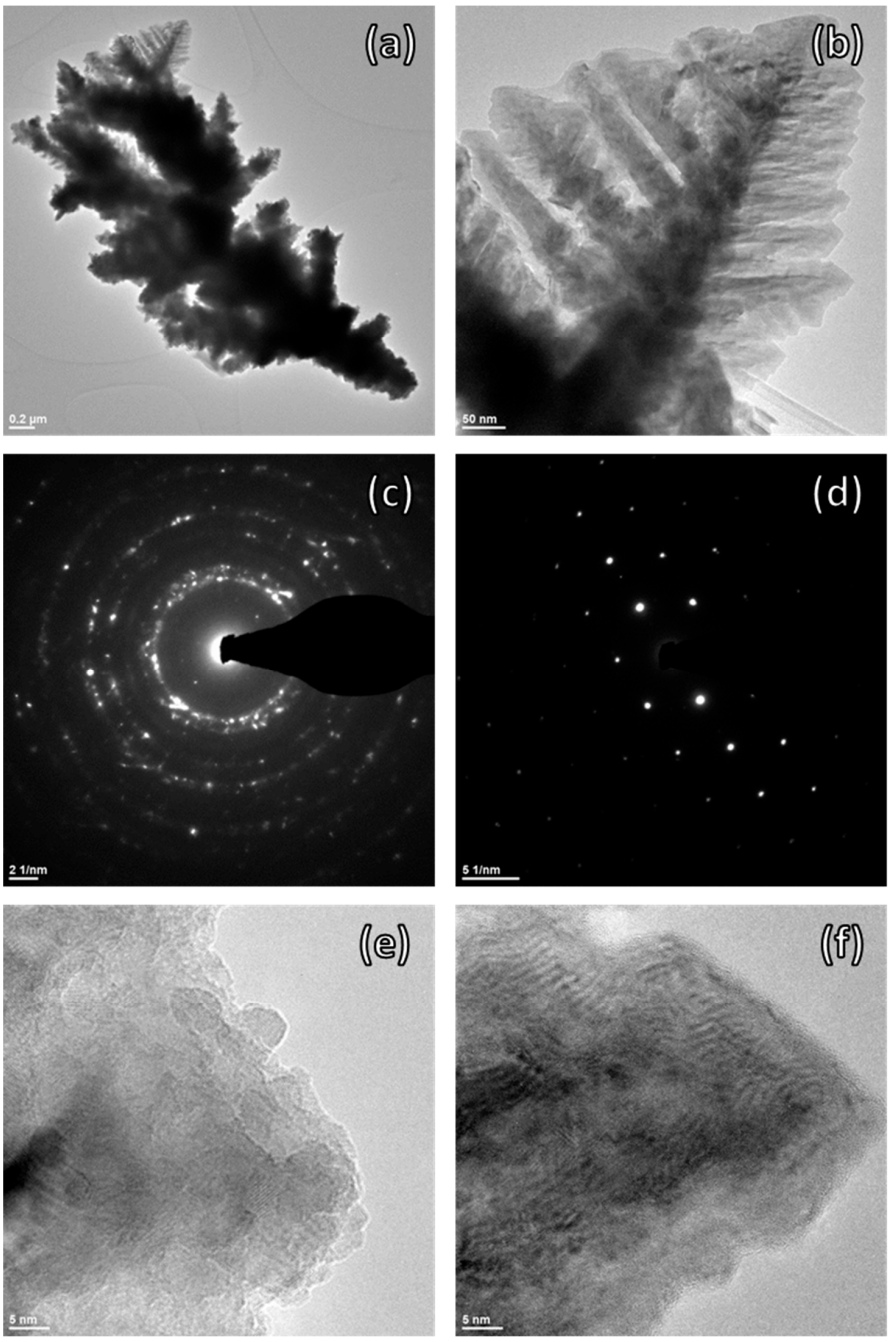


Figure 5. TEM images of Ni-Cu-Fe powder (**a**,**b**); SAED patterns of prepared sample (**c**,**d**); high-resolution TEM images of Ni-Cu-Fe powder showing polycrystalline (**e**) and monocrystal (**f**) areas.

3.4. Electrochemical Measurements

The results of cyclic voltammetry in various concentrations of potassium hydroxide are presented in Figure 6. The lowest peak current density was observed in the most diluted solution of 0.5 M concentration (see Table 2). Increasing the concentration of KOH to 1 M resulted in an increase in the anodic peak current density. Interestingly, further increase led to a decrease in the current density and a higher standard deviation caused by lower repeatability, which is why further studies were conducted in a 1 M KOH solution.

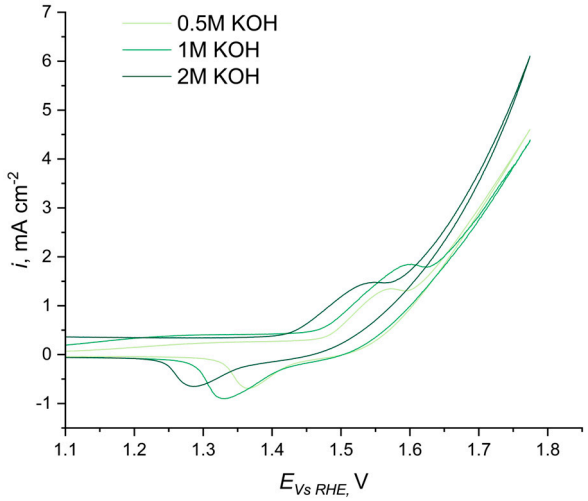


Figure 6. Comparison of the results of CV scans observed for the prepared samples in 0.5, 1, and 2 M KOH solutions.

Table 2. Comparison of the average anodic peak potentials (vs. RHE) and peak current densities observed for prepared samples in KOH solutions of various concentrations.

Solution	E_{pA}, V	i_{pA}, mA cm^{-2}
0.5 M KOH	1.560 ± 0.014	1.12 ± 0.05
1 M KOH	1.563 ± 0.029	1.42 ± 0.07
2 M KOH	1.529 ± 0.019	1.34 ± 0.17

The concentration of KOH, more precisely addressing the concentration of OH^- ions, is crucial for the activity of Ni-based catalysts due to the mechanism of their activity. After immersion into an alkaline solution, nickel hydroxide is formed, which later after polarization to its proper potential contributes to the formation of nickel oxyhydroxide, with nickel in the III valent state being the active centre for the catalysed reaction of the oxidation of simple organic molecules, such as urea.

Even more precisely speaking, during the catalysed reaction, the system needs to maintain the delicate balance between the urea and OH^- ion adsorption on the surface of the catalytic material. A too-low OH^- ion concentration causes a surface blockade with adsorbed urea without enough OH^- ions to oxidize it. If the balance is deviated in the other direction, meaning that on the electrode surface more hydroxide ions are adsorbed than urea particles, the number of exchanged electrons is lower, which results in the generation of less power by the fuel cell [32,33].

In Figure 7, a representative result of cyclic voltammetry studies of material activity toward urea oxidation is presented. The observed anodic peak current density (Table 3) is much higher than that observed in the 1 M KOH solution, which means that the prepared material is active toward urea oxidation [34].

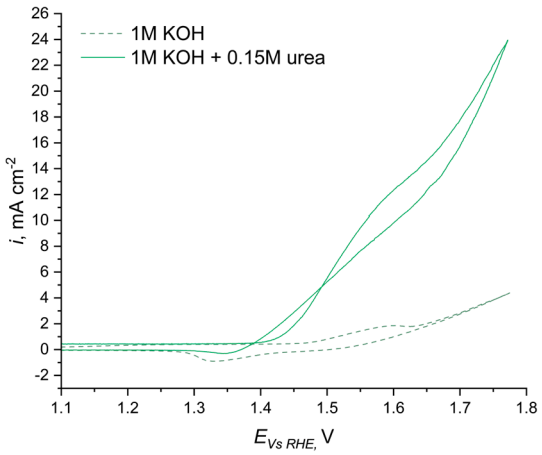


Figure 7. Comparison of the cyclic voltammograms observed for the Ni-Cu-Fe sample in the 1 M KOH solution with and without the addition of 0.15 M urea.

During the anodic scan, nickel, as well as copper and iron, are forming oxyhydroxides, which are active sites for the urea oxidation (Equations (2) and (3)) [35–37]:

$$Ni(OH)_2 + OH^- \rightarrow NiOOH + H_2O \quad (2)$$

$$NiOOH + CO(NH_2)_2 \rightarrow Ni(OH)_2 + prodcuts \quad (3)$$

The products of the UOR depend on the reaction conditions and the electrode material used [26,38].

As a result of product desorption in the voltage range related to the reaction shown in Equation (2), nickel hydroxide is being oxidized back into the oxyhydroxide and can oxidise another freshy adsorbed molecule of urea. Such a cycle of reactions can occur as long as the system is in the proper voltage range and there is enough reaction substrate in the system.

In Figure 7, two anodic peaks are observed, during both forward and reverse scans. Such a shape of a CV curve can be ascribed to the oxidation of freshly adsorbed urea during the reverse scan or to the oxidation of some intermediate chemicals formed during the forward scan, but they were not fully oxidized due to the potential swap. During the reverse scan, a cathodic peak is observed in the same potential region as in the 1 M KOH solution, but it is lower than in case of the solution without the addition of urea. This difference is probably related to the fact that nickel oxyhydroxide formed during the forward scan, being the active agent for the urea oxidation reaction (UOR); however, it then got reduced, which is why the peak related to its reduction is lower than in the case of the solution without the addition of urea.

Table 3. The observed anodic peak current density and peak potential (vs. RHE) values observed for the Ni-Cu-Fe samples compared with other materials.

Sample	E_{pA}, V	i_{pA}, mA cm^{-2}	Reference
NiCu 20	1.731	3.92	[26]
NiCuGO 20	1.736	5.88	[26]
CNT/C@FeN	1.500	3.50	[39]
$Ni_{0.9}Cu_{0.1}$	1.595	32.00	[40]
NiO/Gt 15	1.665	17.63	[41]
Ni@C	1.625	30.30	[9]
Ni-NiO/Gr-450 °C	1.525	38.24	[42]
NiCu/ZnO@MWCNTs	1.405	30.02	[43]
Ni@GO	1.475	17.10	[44]
Ni-Cu-Fe	1.695 ± 0.05	11.98 ± 0.00	In this work

GO—graphene oxide; Gt—graphite planes; Gr—graphene; MWCNT—multiwalled carbon nanotubes.

When comparing the prepared material with a similarly prepared NiCu powder catalyst and NiCuGO composite catalyst, we observed that not only was the average anodic peak potential lower, but also the peak current density registered for the Ni-Cu-Fe material was almost two times higher than for the NiCuGO composite and more than three times higher than that of NiCu material, without the addition of iron [26]. This observation suggests that the addition of iron can increase the activity of the material more efficiently with respect to the nanocarbon in the form of graphene oxide. Its presence increased the NiCu activity more efficiently than the addition of inert but well-conducting graphene oxide (GO), suggesting that the presence of iron increases the material's activity not only due to Fe conductivity, which has been observed before [45], but also due to its catalytic activity toward urea oxidation.

Electrochemical Impedance Spectroscopy comparisons between nano-sized NiFe and NiCu catalysts have shown that the urea oxidation reaction was related to lower charge transfer resistance, which means that the UOR resistance was smaller on NiFe, which explains its higher activity [34,45].

Despite that the addition of an iron NiCu electrocatalyst is still not as active as other electrocatalysts described in the literature (Table 4), a further increase in its activity can be achieved by decreasing the particle size, changing the iron content to a more beneficial Ni:Fe ratio, or adding another element, i.e., Ti [46]. P [47], F [48], S [49], or B [50].

Table 4. Comparison of the activity of different materials by comparing the potentials (vs. RHE) required for the desired current density.

Material	*E*@10 mA cm^{-2}, $V_{vs\ RHE}$	Urea Concentration, mol dm^{-3}	Ref.
NiCuGO20	1.720	0.15	[26]
NiCu20	1.750	0.15	
NiFeOH	1.47 for 50 mAcm^{-2}	0.33	[51]
Ni-WO_x	1.60 for 440 mA cm^{-2}	0.33	[52]
FeNi—oxide 2	1.380	0.33	[53]
Fe-Ni/NF	1.350	0.33	[45]
NiFe-F-4	1.44 for 50 mA cm^{-2}	0.33	[48]
Fe-NiB	1.290	0.5	[50]
Nickel carbonate	1.60 for 117.7 mA cm^{-2}	0.33	[54]
NiO_x/CN_x	1.380	0.33	[10]
Fe(EDTA)-Ni_3S_2 @NF	1.36 for 50 mA cm^{-2}	0.33	[55]
NiOOH/(LDH/αFeOOH)	1.350	0.33	[56]
$Ni_2Fe(CN)_6$	1.35 for 100 mA cm^{-2}	0.33	[57]
Ni-SO_x	1.65 for 323.4 mA cm^{-2}	0.33	[58]
Ir-NiFe-OH	1.38 for 100 mA cm^{-2}	0.33	[13]
NiFeTiS	1.36 for 100 mA cm^{-2}	0.33	[46]
Fe-Ni_3S_2/NF	1.3200	0.33	[45]
O_V-NiFe-LDH	1.300	0.33	[59]
NiFeP	1.397	0.33	[47]
NiFe	1.462	0.33	[47]
Ni-Cu-Fe	1.650 ± 0.060	0.15	In this research

The addition of iron has been proven to increase the activity of nickel electrocatalysts toward urea oxidation [45,50,53,59]. The proposed reason for this phenomenon is the stronger adsorption of urea at NiOOH active sites caused by the presence of iron, which at the same time balances the adsorption energy for intermediate products, decreasing the activation energy for NiFe urea oxidation [50]. Iron has also been proven to have a higher affinity for carbon-based urea oxidation intermediates, leading to the faster release of Ni active sites and increasing the overall reaction rate [49,50]. Another reason for the increased activity of Ni-based electrocatalysts after doping with iron is their lower charge transfer resistance [45,50,53,59].

3.5. EIS

As visible in Figure 8, in both solutions, two characteristic semicircles related to two time constants are observed. Such a shape can be attributed to the equivalent circuit, which is shown in Figure 8 and is typical for electrocatalytic reactions measured for samples prepared by drop-casting [39].

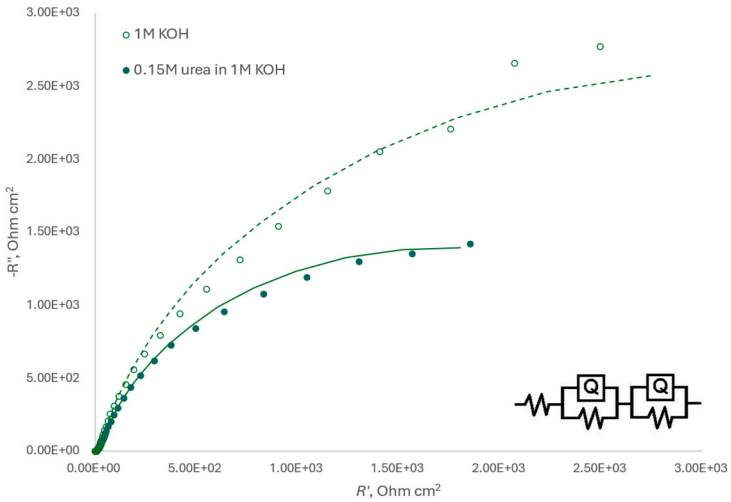


Figure 8. Nyquist plots recorded during the Electrochemical Impedance Spectroscopy investigation of the proposed material in 1 M KOH and in 1 M KOH with the addition of a 0.15 M urea solution with a graphical representation of the electrical equivalent circuit ([R(QR)(QR)]) used for the fitting.

At the beginning of the equivalent circuit, the resistance related to used aqueous solution used is measured (R_s); after that, the solution needs to diffuse through not only an electrical double layer formed after sample polarization but also through the outer layer of the electrocatalytic material deposited on the glassy carbon electrode. The final resistance is related to the charge transfer during the redox reaction (R_{CT}).

The addition of urea into the 1 M KOH solution resulted in a slight increase in the solution resistivity and an increase in the resistance related to the diffusion through the material (R_{dif}), which is caused by the bigger size of the urea particles compared to the hydroxide ions.

As expected, after the observation of higher anodic peak current densities during the CV scans, the charge transfer resistance (R_{CT}) was lower during the urea oxidation reaction (Table 5), which confirms that proposed material exhibits better electrocatalytic properties in the UOR than in water splitting [60].

Table 5. Parameters of the equivalent circuit used for EIS data fiting.

Circuit Element	1 M KOH	0.15 M Urea in 1 M KOH
R_s, Ohm cm^2	2.85 ± 0.04	3.18 ± 0.04
Q-Yo	$2.21 \pm 0.10 \times 10^{-3}$	$2.47 \pm 0.74 \times 10^{-3}$
Q-n	$8.74 \pm 5.00 \times 10^{-1}$	$7.55 \pm 1.25 \times 10^{-1}$
R_{dif}, Ohm cm^2	5743.50 ± 601.50	8549.00 ± 5191.00
Q-Yo	$9.78 \pm 2.40 \times 10^{-3}$	$5.77 \pm 5.00 \times 10^{-3}$
Q-n	$4.18 \pm 0.04 \times 10^{-1}$	$5.64 \pm 1.36 \times 10^{-1}$
R_{CT}, Ohm cm^2	31.06 ± 13.70	22.01 ± 17.44

As presented in Figure 9, during 20 subsequent CV scans in the 1 M KOH solution with the addition of 0.15 M urea, the observed peak current density values were similar to those observed during a single CV scan and remained stable during the examination, proving that the material remained stable during the experiments [48].

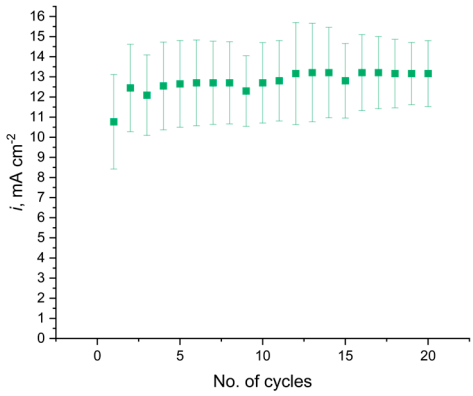


Figure 9. Comparison of the peak current densities observed for Ni-Cu-Fe samples during 20 subsequent CV scans in 1 M KOH solution with the addition of 0.15 M urea.

The material remained active in the course of chronoamperometric polarization as detected through its stable activity, with a typical CA curve for the urea electrocatalyst [20,26,34,45,53]. The observed peaks visible in Figure 10 are related to the formation of the gas bubbles of gaseous reaction products from the electrode surface [20,26,53].

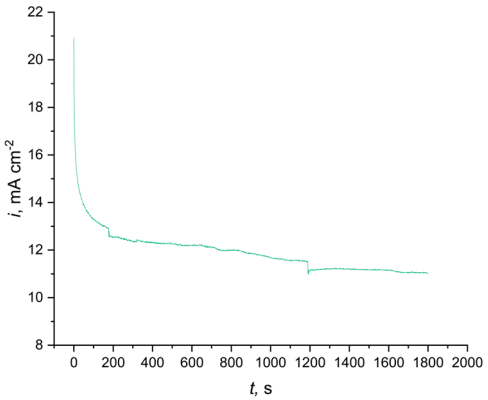


Figure 10. Results recorded during the chronoamperometric study for the sample polarized to the anodic peak potential.

After stabilization (200 s), the observed current density was similar to that observed at the anodic peaks during CV scans of 11.79 ± 1.57 mA cm^{-2}. After 600 s of polarization, the observed average current density was 12.23 ± 1.79 mA cm^{-2}, which is 104% of the initial value observed after the stabilization. At 1000 s of polarization, the observed average current density increased to 12.54 ± 0.8 mA cm^{-2}, which is 106% of the initial value. At the end of the polarization, the observed average current density was 11.88 ± 1.37 mA cm^{-2}, which is 101% of the average current density observed after the stabilization, which means that the proposed material remained stable during the examination. Such an increase in the current density observed for the material is most likely related to the oxidation of UOR intermediates adsorbed at the material surface at the beginning of polarization and as a result of the adsorption of a fresh portion of reaction substrates.

To examine the stability of the newly proposed Ni-Cu-Fe electrocatalyst, the samples were polarized to a current density of 10 mA cm^{-2}, and the resulting voltage is presented in Figure 11. In the course of polarization, which was 3 h, the observed potential varied over a narrow range of 2.36–2.37 $V_{vs\ RHE}$, which ascertained an acceptable stability for the developed electrocatalyst.

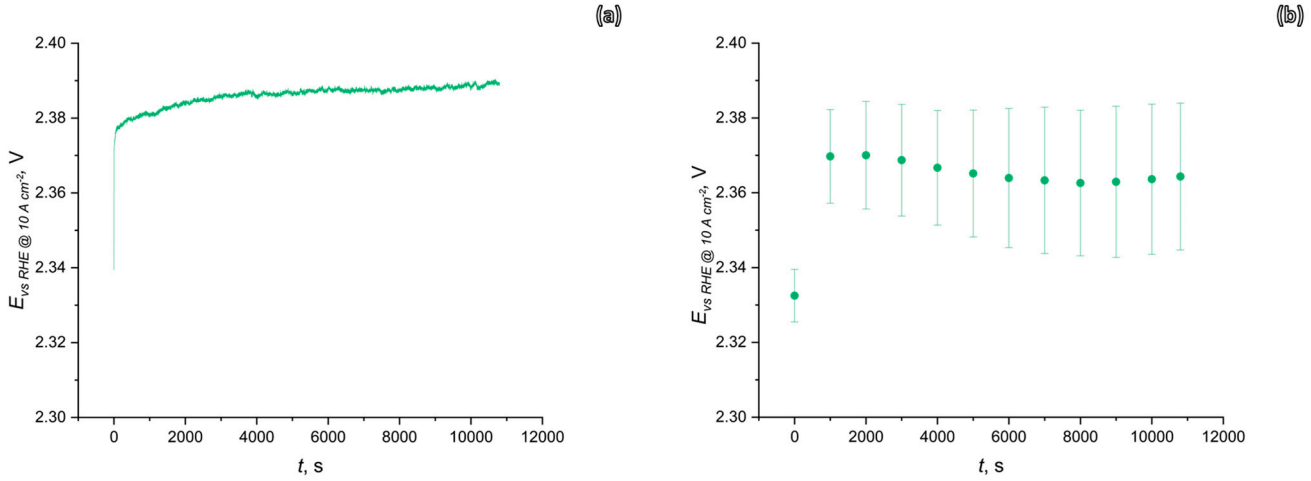


Figure 11. Comparison of the potential required for the current density of 10 mA cm^{-2}: representative example (**a**) and average values (**b**).

4. Conclusions

A simple, quick, and facile process of electrodeposition, which was kept under control, was used in the formation and collection of ternary Ni-Cu-Fe powders within an electrolytic bath with an optimized composition. As trackable evidence, all the metals presented in the electrolytic bath before the synthesis was run were detected in the obtained material, typical of the formation of a Ni-Cu-Fe complex. The prepared powder was observed under a microscope and a characteristic coral-like morphology was scanned, which poses the potential value of this ternary metallic structure for electrocatalytic applications. The obtained Ni-Cu-Fe powder was electroactive in an alkaline environment and revealed activity towards urea oxidation. To realize such a claim, the activity of the prepared material was measured, which was greater than the activity of Ni-Cu powder doped with graphene oxide. This meant that the incorporation of Fe as the tertiary metallic component into the Ni-Cu was a proper tactic for enhancing the efficiency of this hybrid structure when compared with carbon nanoforms like graphene oxide. We have to outline that the activity of the formulated material was lower than that of some of the counterparts or parent structures described in the literature; however, our ternary material was obtained through a versatile, quick, and simple method, which might be applied in developing electrocatalytic materials. However, this must be after its activity is increased upon further assessments in future research programs.

Author Contributions: Conceptualization, M.W.-K. and W.S.; methodology, M.W.-K. and W.S.; software, M.W.-K.; formal analysis, W.S.; investigation, M.W.-K., A.G., A.M., S.S. and A.K.-K.; resources, M.W.-K.; data curation, A.G., A.M., S.S. and A.K.-K.; writing—original draft preparation, M.W.-K. and S.S.; writing—review and editing, M.W.-K. and W.S.; supervision, M.B. and W.S.; project administration, W.S.; funding acquisition, M.W.-K. All authors have read and agreed to the published version of the manuscript.

Funding: This research received no external funding.

Data Availability Statement: The data presented in this study are available on request from the corresponding author. The data are not publicly available due to privacy ethical restrictions.

Conflicts of Interest: The authors declare no conflicts of interest.

References

1. Bacon, F.T. Fuel cells, past, present and future. *Electrochim. Acta* **1969**, *14*, 569–585. [CrossRef]
2. Pramuanjaroenkij, A.; Kakaç, S. The fuel cell electric vehicles: The highlight review. *Int. J. Hydrogen Energy* **2023**, *48*, 9401–9425. [CrossRef]

3. Crespo Parrondo, A.; McPhie, T. Zero emission vehicles: First 'Fit for 55' deal will end the sale of new CO_2 emitting cars in Europe by 2035. *Eur. Comm.—Press Release* **2022**, IP/22/6462. Available online: https://ec.europa.eu/commission/presscorner/detail/en/ip_22_6462 (accessed on 22 May 2024).
4. Wolf, D.D.; Smeers, Y. Comparison of Battery Electric Vehicles and Fuel Cell Vehicles. *World Electr. Veh. J.* **2023**, *14*, 262. [CrossRef]
5. Halder, P.; Babaie, M.; Salek, F.; Shah, K.; Stevanovic, S.; Bodisco, T.A.; Zare, A. Performance, emissions and economic analyses of hydrogen fuel cell vehicles. *Renew. Sustain. Energy Rev.* **2024**, *199*, 114543. [CrossRef]
6. Mansor, M.; Timmiati, S.N.; Lim, K.L.; Wong, W.Y.; Kamarudin, S.K.; Nazirah Kamarudin, N.H. Recent progress of anode catalysts and their support materials for methanol electrooxidation reaction. *Int. J. Hydrogen Energy* **2019**, *44*, 14744–14769. [CrossRef]
7. Yuda, A.; Ashok, A.; Kumar, A. A comprehensive and critical review on recent progress in anode catalyst for methanol oxidation reaction. *Catal. Rev.—Sci. Eng.* **2022**, *64*, 126–228. [CrossRef]
8. Sayed, E.T.; Eisa, T.; Mohamed, H.O.; Abdelkareem, M.A.; Allagui, A.; Alawadhi, H.; Chae, K.-J. Direct urea fuel cells: Challenges and opportunities. *J. Power Sources* **2019**, *417*, 159–175. [CrossRef]
9. Tran, T.Q.N.; Park, B.J.; Yun, W.H.; Duong, T.N.; Yoon, H.H. Metal–organic framework–derived Ni@C and NiO@C as anode catalysts for urea fuel cells. *Sci. Rep.* **2020**, *10*, 278. [CrossRef]
10. Shekhawat, A.; Samanta, R.; Panigrahy, S.; Barman, S. Electrocatalytic Oxidation of Urea and Ethanol on Two-Dimensional Amorphous Nickel Oxide Encapsulated on N-Doped Carbon Nanosheets. *ACS Appl. Energy Mater.* **2023**, *6*, 3135–3146. [CrossRef]
11. Chakrabarty, S.; Offen-Polak, I.; Burshtein, T.Y.; Farber, E.M.; Kornblum, L.; Eisenberg, D. Urea oxidation electrocatalysis on nickel hydroxide: The role of disorder. *J. Solid State Electrochem.* **2020**, *25*, 159–171. [CrossRef]
12. Li, J.; Wang, S.; Chang, J.; Feng, L. A review of Ni based powder catalyst for urea oxidation in assisting water splitting reaction. *Adv. Powder Mater.* **2022**, *1*, 100030. [CrossRef]
13. Chen, X.; Wan, J.; Chai, J.; Zhang, L.; Zhang, F.; Zhang, Q.; Gu, L.; Zheng, L.; Yu, R. Nickel-iron in the second coordination shell boost single-atomic-site iridium catalyst for hight-performance urea electrooxidation. *Nano Res.* **2024**, *17*, 3919–3926. [CrossRef]
14. Xie, J.; Qu, H.; Lei, F.; Peng, X.; Liu, W.; Gao, L.; Hao, P.; Cui, G.; Tang, B. Partially amorphous nickel-iron layered double hydroxide nanosheet arrays for robust bifunctional electrocatalysis. *J. Mater. Chem. A* **2018**, *6*, 16121–16129. [CrossRef]
15. Shit, S.; Ghosh, S.; Bolar, S.; Murmu, N.C.; Kuila, T. Understanding the Synergistic Effect in Oxygen Evolution Reaction Catalysis from Chemical Kinetics Point of View: An Iron Oxide/Nickel Oxide Case Study. *J. Electrochem. Soc.* **2020**, *167*, 116514. [CrossRef]
16. Maniam, K.K.; Chetty, R.; Thimmappa, R.; Paul, S. Progress in the Development of Electrodeposited Catalysts for Direct Liquid Fuel Cell Applications. *Appl. Sci.* **2022**, *12*, 501. [CrossRef]
17. Das, M.; Khan, Z.B.; Banerjee, M.; Biswas, A.; Dey, R.S. Three-dimensional nickel and copper-based foam-in-foam architecture as an electrode for efficient water electrolysis. *Catal. Today* **2023**, *424*, 113836. [CrossRef]
18. Wei, H.; Xu, Q.; Li, A.; Wan, T.; Huang, Y.; Cui, D.; Pan, D.; Dong, B.; Wei, R.; Naik, N.; et al. Dendritic core-shell copper-nickel alloy@metal oxide for efficient non-enzymatic glucose detection. *Sens. Actuators B Chem.* **2021**, *337*, 129687. [CrossRef]
19. Ghosh, S.K.; Grover, A.K.; Dey, G.K.; Totlani, M.K. Nanocrystalline Ni-Cu alloy plating by pulse electrolysis. *Surf. Coat. Technol.* **2000**, *126*, 48–63. [CrossRef]
20. Wala, M.M.; Szewczyk, A.K.K. Preparation of NiCuGO composite and investigation of its electrocatalytic properties in methanol oxidation. *Electrochim. Acta* **2022**, *425*, 140743. [CrossRef]
21. Niu, S.; Li, S.; Du, Y.; Han, X.; Xu, P. How to Reliably Report the Overpotential of an Electrocatalyst. *ACS Energy Lett.* **2020**, *5*, 1083–1087. [CrossRef]
22. Plowman, B.J.; Jones, L.A.; Bhargava, S.K. Building with bubbles: The formation of high surface area honeycomb-like films via hydrogen bubble templated electrodeposition. *Chem. Commun.* **2015**, *51*, 4331–4346. [CrossRef] [PubMed]
23. Kozicki, M.N. Information in electrodeposited dendrites. *Adv. Phys. X* **2021**, *6*, 1920846. [CrossRef]
24. Koh, J.H.; Won, D.H.; Eom, T.; Kim, N.K.; Jung, K.D.; Kim, H.; Hwang, Y.J.; Min, B.K. Facile CO_2 Electro-Reduction to Formate via Oxygen Bidentate Intermediate Stabilized by High-Index Planes of Bi Dendrite Catalyst. *ACS Catal.* **2017**, *7*, 5071–5077. [CrossRef]
25. Hu, B.; Yu, J.; Meng, J.; Xu, C.; Cai, J.; Zhang, B.; Liu, Y.; Yu, D.; Zhou, X.; Chen, C. Porous Ni-Cu Alloy Dendrite Anode Catalysts with High Activity and Selectivity for Direct Borohydride Fuel Cells. *ACS Appl. Mater. Interfaces* **2022**, *14*, 3910–3918. [CrossRef] [PubMed]
26. Wala, M.; Blacha–Grzechnik, A.; Stolarczyk, A.; Bajkacz, S.; Dydo, P.; Simka, W. Unexpected electrochemical oxidation of urea on a new NiCuGO composite catalyst. *Int. J. Hydrogen Energy* **2023**, *48*, 34229–34243. [CrossRef]
27. Wu, J.; Chen, J.; Yu, T.; Zhai, Z.; Zhu, Y.; Wu, X.; Yin, S. Boosting Electrochemical Kinetics of $NiCo_2$ via MoO_2 Modification for Biomass Upgrading Assisted Hydrogen Evolution. *ACS Catal.* **2023**, *13*, 13257–13266. [CrossRef]
28. Jiang, W.; Zhuo, X.; Yu, T.; Lu, J.; Zhai, Z.; Wen, H.; Yin, S. Regulating Reaction Intermediate Adsorption of $Co_{0.5}NiS_2$-Ni_3S_2 Nanorods for Efficient Urea Electrolysis. *ACS Sustain. Chem. Eng.* **2024**, *12*, 998–1006. [CrossRef]
29. Feng, B.; Jiang, W.; Deng, R.; Lu, J.; Tsiakaras, P.; Yin, S. Agglomeration inhibition engineering of nickel–cobalt alloys by a sacrificial template for efficient urea electrolysis. *J. Colloid Interface Sci.* **2024**, *663*, 1019–1027. [CrossRef]
30. Sun, H.; Li, L.; Chen, Y.; Kim, H.; Xu, X.; Guan, D.; Hu, Z.; Zhang, L.; Shao, Z.; Jung, W.C. Boosting ethanol oxidation by NiOOH-CuO nano-heterostructure for energy-saving hydrogen production and biomass upgrading. *Appl. Catal. B Environ.* **2023**, *325*, 122388. [CrossRef]
31. Taffa, D.H.; Balkenhohl, D.; Amiri, M.; Wark, M. Minireview: Ni–Fe and Ni–Co Metal–Organic Frameworks for Electrocatalytic Water-Splitting Reactions. *Small Struct.* **2023**, *4*, 2200263. [CrossRef]

32. Shi, W.; Ding, R.; Li, X.; Xu, Q.; Liu, E. Enhanced performance and electrocatalytic kinetics of Ni-Mo/graphene nanocatalysts towards alkaline urea oxidation reaction. *Electrochim. Acta* **2017**, *242*, 247–259. [CrossRef]
33. Mohamed, I.M.A.; Kanagaraj, P.; Yasin, A.S.; Iqbal, W.; Liu, C. Electrochemical impedance investigation of urea oxidation in alkaline media based on electrospun nanofibers towards the technology of direct-urea fuel cells. *J. Alloys Compd.* **2020**, *816*, 152513. [CrossRef]
34. Xu, W.; Du, D.; Lan, R.; Humphreys, J.; Wu, Z.; Tao, S. Highly active Ni-Fe double hydroxides as anode catalysts for electrooxidation of urea. *New J. Chem.* **2017**, *41*, 4190–4196. [CrossRef]
35. Gao, X.; Zhang, S.; Wang, P.; Jaroniec, M.; Zheng, Y.; Qiao, S.Z. Urea catalytic oxidation for energy and environmental applications. *Chem. Soc. Rev.* **2024**, *53*, 1552–1591. [CrossRef]
36. Hopsort, G.; Pereira Do Carmo, D.; Latapie, L.; Groenen Serrano, K.; Tzedakis, T. Progress toward a better understanding of the urea oxidation by electromediation of Ni (II)/Ni (III) system in alkaline media. *Electrochim. Acta* **2023**, *442*, 141898. [CrossRef]
37. Gnana kumar, G.; Farithkhan, A.; Manthiram, A. Direct Urea Fuel Cells: Recent Progress and Critical Challenges of Urea Oxidation Electrocatalysis. *Adv. Energy Sustain. Res.* **2020**, *1*, 2000015. [CrossRef]
38. Tatarchuk, S.W.; Medvedev, J.J.; Li, F.; Tobolovskaya, Y.; Klinkova, A. Nickel-Catalyzed Urea Electrolysis: From Nitrite and Cyanate as Major Products to Nitrogen Evolution. *Angew. Chem. Int. Ed.* **2022**, *61*, e202209839. [CrossRef]
39. Modak, A.; Mohan, R.; Rajavelu, K.; Cahan, R.; Bendikov, T.; Schechter, A. Metal−Organic polymer-derived interconnected Fe−Ni alloy by carbon nanotubes as an advanced design of urea oxidation catalysts. *ACS Appl. Mater. Interfaces* **2021**, *13*, 8461–8473. [CrossRef]
40. Hefnawy, M.A.; Fadlallah, S.A.; El-Sherif, R.M.; Medany, S.S. Synergistic effect of Cu-doped NiO for enhancing urea electrooxidation: Comparative electrochemical and DFT studies. *J. Alloys Compd.* **2021**, *896*, 162857. [CrossRef]
41. Abdel Hameed, R.M.; Medany, S.S. Enhanced electrocatalytic activity of NiO nanoparticles supported on graphite planes towards urea electro-oxidation in NaOH solution. *Int. J. Hydrogen Energy* **2017**, *42*, 24117–24130. [CrossRef]
42. Wang, S.; Xu, P.; Tian, J.; Liu, Z.; Feng, L. Phase structure tuning of graphene supported Ni-NiO Nanoparticles for enhanced urea oxidation performance. *Electrochim. Acta* **2021**, *370*, 137755. [CrossRef]
43. Basumatary, P.; Konwar, D.; Yoon, Y.S. A novel Ni–Cu/ZnO@MWCNT anode employed in urea fuel cell to attain superior performances. *Electrochim. Acta* **2018**, *261*, 78–85. [CrossRef]
44. Munde, A.V.; Mulik, B.B.; Chavan, P.P.; Sathe, B.R. Hydrothermal Syntheses of NiO−GO Nanocomposite on 3D Nickel Foam as a Support for Pt Nanoparticles and its Superior Electrocatalytic Activity Towards Methanol Oxidation. *Electrochim. Acta* **2020**, *349*, 1484–1493. [CrossRef]
45. Samdani, J.S.; Sanetuntikul, J.; Shanmugam, S. Self-supported iron-doped nickel sulfide as efficient catalyst for electrochemical urea and hydrazine oxidation reactions. *Int. J. Hydrogen Energy* **2022**, *47*, 27347–27357. [CrossRef]
46. Nur Indah Sari, F.; Ke, M.T.; Huang, Y.J.; Zheng, T.M.; Su, Y.H.; Ting, J.M. NiFe sulfide electronic structure modulation via metal doping towards enhanced urea oxidation reaction performance. *Appl. Surf. Sci.* **2024**, *649*, 159187. [CrossRef]
47. Cao, J.; Wang, G.; Hou, S.; Yu, W.; Yang, Z.; Wu, Y. Facile fabrication of amorphous NiFeP nanosheets to promote urea oxidation reaction for energy-saving hydrogen production. *J. Mater. Sci.* **2023**, *58*, 16019–16032. [CrossRef]
48. Wang, K.; Hou, M.; Huang, W.; Cao, Q.; Zhao, Y.; Sun, X.; Ding, R.; Lin, W.; Liu, E.; Gao, P. F-decoration-induced partially amorphization of nickel iron layered double hydroxides for high efficiency urea oxidation reaction. *J. Colloid Interface Sci.* **2022**, *615*, 309–317. [CrossRef]
49. Peng, K.; Liu, L.; Bhuvanendran, N.; Qiao, F.; Lei, G.; Lee, S.Y.; Xu, Q.; Su, H. Effective regulation on catalytic performance of nickel-iron-vanadium layered double hydroxide for urea oxidation via sulfur incorporation. *Mater. Adv.* **2023**, *4*, 1354–1362. [CrossRef]
50. Chen, Z.; Zheng, R.; Zou, H.; Wang, R.; Huang, C.; Dai, W.; Wei, W.; Duan, L.; Ni, B.J.; Chen, H. Amorphous iron-doped nickel boride with facilitated structural reconstruction and dual active sites for efficient urea electrooxidation. *Chem. Eng. J.* **2023**, *465*, 142684. [CrossRef]
51. Babar, P.; Patil, K.; Lee, D.M.; Karade, V.; Gour, K.; Pawar, S.; Kim, J.H. Cost-effective and efficient water and urea oxidation catalysis using nickel-iron oxyhydroxide nanosheets synthesized by an ultrafast method. *J. Colloid Interface Sci.* **2021**, *584*, 760–769. [CrossRef]
52. Wang, L.; Zhu, Y.; Wen, Y.; Li, S.; Cui, C.; Ni, F.; Liu, Y.; Lin, H.; Li, Y.; Peng, H.; et al. Regulating the Local Charge Distribution of Ni Active Sites for the Urea Oxidation Reaction. *Angew. Chem.* **2021**, *133*, 10671–10676. [CrossRef]
53. Gu, X.; Yang, D.; Liu, Z.; Wang, S.; Feng, L. Iron oxide promoted nickel/nickel oxide rough nanorods for efficient urea assisted water splitting. *Electrochim. Acta* **2020**, *353*, 136516. [CrossRef]
54. Liu, H.; Wang, P.; Qi, X.; Liu, J.; Yin, A.; Wang, Y.; Ye, Y.; Luo, J.; Ren, Z.; Yu, S.; et al. An amorphous nickel carbonate catalyst for superior urea oxidation reaction. *J. Electroanal. Chem.* **2023**, *949*, 117856. [CrossRef]
55. Lv, W.; Zhu, L.; Kong, X.; Shi, H.; Wang, C.; Zhang, R.; Wang, W. Enhancement effects of Fe-doped Ni_3S_2 on efficient electrochemical urea oxidation and mechanism insights. *J. Alloys Compd.* **2023**, *965*, 171292. [CrossRef]
56. Cai, M.; Zhu, Q.; Wang, X.; Shao, Z.; Yao, L.; Zeng, H.; Wu, X.; Chen, J.; Huang, K.; Feng, S. Formation and Stabilization of NiOOH by Introducing α-FeOOH in LDH: Composite Electrocatalyst for Oxygen Evolution and Urea Oxidation Reactions. *Adv. Mater.* **2023**, *35*, 2209338. [CrossRef]

57. Geng, S.K.; Zheng, Y.; Li, S.Q.; Su, H.; Zhao, X.; Hu, J.; Shu, H.B.; Jaroniec, M.; Chen, P.; Liu, Q.H.; et al. Nickel ferrocyanide as a high-performance urea oxidation electrocatalyst. *Nat. Energy* **2021**, *69*, 904–912. [CrossRef]
58. Gao, X.; Bai, X.; Wang, P.; Jiao, Y.; Davey, K.; Zheng, Y.; Qiao, S.Z. Boosting urea electrooxidation on oxyanion-engineered nickel sites via inhibited water oxidation. *Nat. Commun.* **2023**, *14*, 5842. [CrossRef]
59. Liu, G.; Xie, C.; Zhang, Y.; Du, Y.; Wang, J.; Lin, J.; Bai, J.; Li, J.; Zhou, C.; Zhou, T.; et al. Synergistic etching of nickel foam by Fe3+ and Cl− ions to synthesize nickel-iron-layered double hydroxide nanolayers with abundant oxygen vacancies for superior urea oxidation. *J. Colloid Interface Sci.* **2024**, *668*, 375–384. [CrossRef]
60. Golmohammadi, F.; Amiri, M. Facile synthesis of nanofiber composite based on biomass-derived material conjugated with nanoparticles of Ni–Co oxides for high-performance supercapacitors. *J. Mater. Sci. Mater. Electron.* **2020**, *31*, 2269–2279. [CrossRef]

Disclaimer/Publisher's Note: The statements, opinions and data contained in all publications are solely those of the individual author(s) and contributor(s) and not of MDPI and/or the editor(s). MDPI and/or the editor(s) disclaim responsibility for any injury to people or property resulting from any ideas, methods, instructions or products referred to in the content.